Exp Fluids (2015) 56:193
DOI 10.1007/s00348-015-2057-9

RESEARCH ARTICLE

Characterization of scalar mixing in dense gaseous jets using X-ray computed tomography

Jared Dunnmon[1] · Sadaf Sobhani[1] · Tae Wook Kim[2] · Anthony Kovscek[2] · Matthias Ihme[1]

Received: 26 May 2015 / Revised: 3 September 2015 / Accepted: 5 September 2015 / Published online: 26 September 2015

Abstract An experimental technique based on X-ray computed tomography (XCT) is used to characterize scalar mixing of a krypton jet with air at turbulent conditions. The high radiodensity of the krypton gas enables non-intrusive volumetric measurements of gas density and mixture composition based on spatial variations in X-ray attenuation. Comparisons of these measurements to both computational results from large-eddy simulations and data from previous experiments are presented, and the viability of this diagnostic technique is assessed. Important aspects of X-ray attenuation theory, XCT practice, and relevant error analysis are considered in data processing, and their impacts on the future development of this technique are discussed.

List of symbols

δ	Dirac delta function
γ	X-ray spectrum density function
κ	Wavenumber
$\mathcal{F}_\alpha(q)\{\psi\}$	α-Dimensional Fourier transform of function ψ with respect to q
μ	Linear attenuation coefficient
ν	Kinematic viscosity
ϕ	Scan angle
ρ	Density
σ	Standard deviation
τ	Timescale
ξ	Mass attenuation coefficient
ζ	Jet buoyancy parameter
D	Diameter
E	X-ray energy
Fr	Froude number
g	X-ray projection; gravitational acceleration
I	Intensity
K	Number of energy levels
L	Integral length scale
l	Axis parallel to source plane
N	Number of compounds
n	Number of samples
P	Pressure
r	Radial coordinate
R_u	Universal gas constant
Re	Reynolds number
s	Axis perpendicular to source plane
SE	Standard error
T	Temperature
u	Axial velocity
W	Molar mass
X	Mole fraction
x, y, z	Cartesian coordinate system
Y	Mass fraction

Subscripts and accents

0	X-ray source location
$\bar{\ }$	Spectral average
$\hat{\ }$	Fourier transform
∞	Far-field condition
$\langle\cdot\rangle$	Arithmetic average
Bk	Background
C	Centerline
d	X-ray detector location
E	Turbulent eddy
M	Mixture

✉ Jared Dunnmon
jdunnmon@stanford.edu

1 Department of Mechanical Engineering, Stanford University, Stanford, CA, USA

2 Department of Energy Resources Engineering, Stanford University, Stanford, CA, USA

Meas	Measured data quantity
o	Jet orifice condition
T	Turbulent

1 Introduction

Measurements of scalar mixing in fluid mechanics have become an important tool in understanding the structure of a wide variety of flow phenomena. In particular, scalar concentration measurements in turbulent gas-phase shear flows have yielded both quantitative and qualitative information that has significantly enhanced fundamental understanding of the underlying flow physics. While common methods such as Schlieren imaging (Crow and Champagne 1971; Meier 2002), Rayleigh scattering (Dowling and Dimotakis 1990; Pitts 1991; Richards and Pitts 1993; Su et al. 2010), Raman scattering (Birch et al. 1978), and planar laser-induced fluorescence (Hiller and Hanson 1988) reliably yield pointwise or two-dimensional results, advances in computational capabilities and design complexity have lent increased importance to the development of three-dimensional field data for transported scalars.

Current options for three-dimensional visualization of scalar quantities are limited, and the majority of this work is accomplished via various types of optical tomography. Optical tomographic methods were first proposed by Stuck (1977) and Byer and Shepp (1979) for determining spatial concentration of air pollutants via tomographic reconstruction of laser absorption data. In the nearly 40 years since, methods such as holographic interferometry (Feng et al. 2002; Snyder and Hesselink 1988; Watt and Vest 1990), laser absorption (Bennett and Byer 1984; Lavinskaya et al. 2006; Mohamad et al. 2006; Santoro and Semerjian 1981; Wright et al. 2006), chemiluminescence (Floyd et al. 2011), and rainbow Schlieren (Agrawal et al. 1997) have all been used in combination with tomographic reconstruction algorithms to yield three-dimensional scalar field data in gas-phase applications.

While optical tomographic methods have performed well in many situations, there exist a wide variety of optically inaccessible flow geometries for which they would not be applicable. The general approach to this problem has been attempting to artificially design optical access ports into experimental and industrial environments with varying levels of success (Mohamad et al. 2006; Wright et al. 2006). Further, many experimental setups contain equipment that for practical or cost reasons restricts either view number or available view angles, each of which requires the use of limited-view reconstruction algorithms that are not always as accurate as those used in the high-view limit (Elsinga et al. 2006; Floyd et al. 2011; Lavinskaya et al. 2006; Prince and Links 2006). In an ideal case, one would be able to obtain quantitative data for scalar quantities in optically inaccessible gas-phase flow environments without resorting to either of these limited-view techniques.

A potential avenue for accomplishing this goal that remains as yet unexplored involves the consideration of clinical X-ray computed tomography (XCT) systems. These devices were fundamentally designed to image internal structures through an optically opaque outer shell, and similar systems have already been successfully utilized to measure mean flow structures in the context of fuel sprays and multiphase flows (Chaouki et al. 1997; Coletti et al. 2014; Escudero and Heindel 2014; Linne 2013). The recent work of Heindel (2011) provides a detailed overview of applications of X-ray diagnostics to multiphase flows, with a substantial emphasis on tomographic methods.

While the same principle could be applied to optically inaccessible gas-phase flow phenomena, the major reason that clinical XCT systems have not been used to study dynamic gas-phase flow phenomena is that gases are extremely non-attenuative to photons at commonly used medical X-ray energies, rendering X-ray absorption measurements impractical for most gases using these systems. In contrast, soft X-rays from low-energy coherent synchrotron radiation represent a more typical source for X-ray measurements of gas-phase phenomena (Frank et al. 2014). The work of Kastengren and Powell (2014) highlights the potential advantages of synchrotron sources over laboratory-scale X-ray sources in providing bright, monochromatic beams. However, synchrotron sources are not generally designed for use in three-dimensional tomographic techniques, making laboratory-scale sources preferable for demonstrating the application of XCT to gas-phase flows. X-ray fluorescence techniques have also been investigated for application to visualization of turbulent gas-phase mixing and are effective even with weakly absorbing samples (Kastengren et al. 2011). These techniques also require a specialized low-energy X-ray source and are thus not generally used in three-dimensional tomographic applications.

In this study, we develop a method for measuring scalar fields of a turbulent gaseous jet using widely available clinical XCT technology. Tomographic reconstruction of carefully acquired X-ray attenuation data using inbuilt scanner software yields easily attainable measurements of the mean scalar concentration field in three dimensions with high spatial resolution. The coupling of this high spatial granularity with both rapid scan times and the feasibility of measurements in optically inaccessible environments gives XCT several unique advantages in the context of gas-phase flow diagnostics. This paper will proceed by first exploring the theory behind XCT and unique aspects of its application to gas-phase phenomena in Sect. 2. Section 3 will discuss critical aspects of experimental design, calibration, and uncertainty analysis before results from both experiment and computation are compared and contrasted in Sect. 4. Finally, Sect. 5 will summarize key conclusions and propose future directions for work in gas-phase XCT.

2 Theory of gas-phase XCT

2.1 Fundamentals of X-ray attenuation

X-ray absorption diagnostics are enabled by the fact that X-ray photons are attenuated when they interact with matter. The fundamental difference between the X-ray diagnostics under consideration here and the laser diagnostics often used for gas-phase flow diagnostics is that X-ray photons primarily interact with both outer and core electrons via mechanisms including Rayleigh scattering, the photoelectric effect, and Compton scattering, whereas laser diagnostics are dominated by scattering interactions with valence electrons (Bushberg et al. 2011). In general, the intensity of photons measured at the detector after passing through an object, I_{d}, can be related to the intensity of photons emitted from a source, I_0, via the Beer–Lambert law (Macovski 1983),

$$\frac{I_{\mathrm{d}}}{I_0} = e^{-\int \mu(s)\mathrm{d}s}, \tag{1}$$

where s is the path length through the object and μ is its linear attenuation coefficient. This attenuation coefficient may be expressed as the following product of the mass attenuation coefficient ξ and its density ρ,

$$\mu = \xi\rho, \;\; \text{with} \;\; \xi = \left(\frac{\mu}{\rho}\right), \tag{2}$$

where ξ is a nonlinear function of the photon energy that varies with material composition. Note that ξ is most fundamentally an atomic quantity that increases with atomic number (as a proxy for electron density), and can be determined via measurements of both μ and ρ at reference conditions (Bushberg et al. 2011; Macovski 1983). In general, values of the mass attenuation coefficient ξ are only tabulated for monoenergetic sources, whereas most X-ray sources emit a polyenergetic photon spectrum. Thus, one must take the spectral average of the mass attenuation coefficient to obtain an accurate effective value for ξ. The spectrally averaged mass attenuation coefficient for a polyenergetic scan, $\bar{\xi}$, can be determined as,

$$\bar{\xi} = \int \gamma(E)\xi(E)\mathrm{d}E, \tag{3}$$

where E is the photon energy and $\gamma(E)$ is the spectral probability density function. Accurate $\bar{\xi}$ values would be necessary for a first-principles quantitative analysis of XCT data from a given X-ray facility, each of which will have its own characteristic $\gamma(E)$. Further discussion on this point can be found in Sect. 3.

2.2 X-ray computed tomography: a review

X-ray computed tomography refers to the process of reconstructing a two-dimensional field function from its integral X-ray absorption projections in two dimensions. The projection function $g(l,\phi)$ can be written in terms of ϕ, the angle between the horizontal and the source-detector axis, and l, the coordinate parallel to the detector plane (Prince and Links 2006),

$$g(l,\phi) = \int \rho(s(l,\phi))\bar{\xi}(s(l,\phi))\mathrm{d}s. \tag{4}$$

To implement the XCT imaging procedure, a source-detector assembly is, for instance, rotated around the sample and the projection function is sampled at a collection of angles that depends on the scanner geometry (Macovski 1983). The sinogram representing $g(l,\phi)$ can then be defined as the Radon transform of the attenuation field function $\mu(x,y)$,

$$g(l,\phi) = \iint \mu(x,y)\delta(x\cos\phi + y\sin\phi - l)\mathrm{d}x\mathrm{d}y, \tag{5}$$

where δ is the Dirac delta function, x is the horizontal in-plane coordinate, and y is the vertical in-plane coordinate as shown in Fig. 1. Note that Eq. (5) represents the expression appropriate for a simple, monoenergetic, parallel-beam geometry. While results in this paper will be presented in this context for simplicity, most modern scanners use either a fan-beam or a cone-beam geometry, which would give similar, but more complex expressions (Prince and Links 2006). The inverse Radon transform required to reconstruct $\mu(x,y)$ from $g(l,\phi)$ is generally performed by native scanner software. It relies on the well-known projection-slice theorem to relate $g(l,\phi)$ and $\mu(x,y)$ in the following manner in terms of $\hat{G}(\kappa,\phi)$, the one-dimensional Fourier transform of the projection function with respect to l, and the spatial wavenumber κ (Macovski 1983; Prince and Links 2006),

$$\begin{aligned}
\hat{G}(\kappa,\phi) &= \mathcal{F}_{1D}(l)\{g(l,\phi)\},\\
&= \int g(l,\phi)e^{-2i\pi\kappa l}\mathrm{d}l,\\
&= \iiint \mu(x,y)\delta(x\cos\phi + y\sin\phi - l)e^{-2i\pi\kappa l}\mathrm{d}x\mathrm{d}y\mathrm{d}l,\\
&= \iint \mu(x,y)e^{-2i\pi\kappa(x\cos\phi + y\sin\phi)}\mathrm{d}x\mathrm{d}y,\\
&= \mathcal{F}_{2D}(\kappa\cos\phi,\kappa\sin\phi)\{\mu(x,y)\}.
\end{aligned} \tag{6}$$

Figure 1 illustrates this relation graphically.

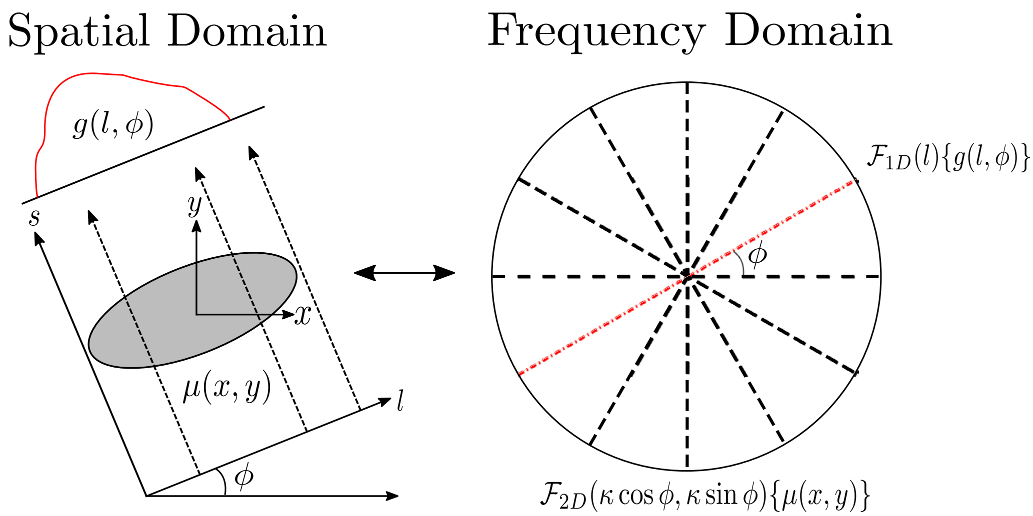

Fig. 1 Graphical illustration of the projection-slice theorem

In the XCT scanner used for this study, the inverse Radon transform required to compute μ from g using Eq. (6) is accomplished via a filtered backprojection method that takes advantage of the projection-slice theorem to express the reconstructed field $\mu(x, y)$ as (Prince and Links 2006),

$$\mu(x, y) = \int_0^{\pi} \int_{-\infty}^{\infty} |\kappa| \hat{G}(\kappa, \phi) e^{2i\pi\kappa l} \mathrm{d}\kappa \mathrm{d}\phi \big|_{l = x\cos\phi + y\sin\phi}, \tag{7}$$

where the ramp filter in κ is introduced to ensure proper relative weighting of low- and high-frequency signals (Prince and Links 2006). In practice, the backprojection operator is applied to each projection individually and the backprojections at all sampled values of ϕ are summed to give the reconstructed attenuation field. Further details on the implementation of XCT and filtered backprojection can be found in Prince and Links (2006), Macovski (1983), or Hsieh (2009). The mathematical methods described above allow for the use of XCT to non-intrusively interrogate the attenuation characteristics of a given sample. Attenuation data from XCT scanners are generally output in terms of Hounsfield units (HU) by normalizing measurements of μ such that a value of 0 corresponds to water and a value of -1000 corresponds to air, following the relation (Prince and Links 2006),

$$\mathrm{HU} = 1000\left(\frac{\mu - \mu_{\mathrm{H_2O}}}{\mu_{\mathrm{H_2O}}}\right). \tag{8}$$

We therefore report attenuation in HU values throughout this study. Three-dimensional images are formed by stacking multiple two-dimensional slices taken in succession. The following sections demonstrate how such data can be used in combination with well-known physical relations to obtain useful information about gas-phase fluid phenomena.

2.3 Quantitative analysis of gas-phase XCT

In this study, we consider an inert binary mixture at known pressure P and temperature T. We utilize the attenuation mixture rule to write the mixture mass attenuation coefficient as (Jackson and Hawkes 1981; Macovski 1983; Thompson and Vaughan 2005),

$$\frac{\bar{\mu}_M}{\rho} = \sum_{j=1}^{N} \bar{\xi}_j Y_j, \tag{9}$$

with ρ the mixture density, $\bar{\mu}_M$ the mixture linear attenuation, Y_j the mass fraction of component j, and N the number of components in the mixture. Rewriting the mass fraction in terms of a partial density ρ_j and utilizing the ideal gas law along with Dalton's law gives,

$$\bar{\mu}_M = \sum_{j=1}^{N} \bar{\xi}_j \rho_j = \frac{P}{R_{\mathrm{u}} T} \sum_{j=1}^{N} \bar{\xi}_j X_j W_j, \tag{10}$$

taking W_j as the molar mass of species j, R_{u} as the universal gas constant, and X_j as the mole fraction. Rearranging the above expression, writing out the summation for a two-component mixture, and solving for the mole fraction of component 1 in terms of the mixture attenuation $\bar{\mu}_M$ yields,

$$X_1 = \frac{\bar{\mu}_M - \frac{PW_2}{R_{\mathrm{u}}T}\bar{\xi}_2}{\frac{PW_1}{R_{\mathrm{u}}T}\bar{\xi}_1 - \frac{PW_2}{R_{\mathrm{u}}T}\bar{\xi}_2}, \tag{11}$$

which expresses X_1 in terms of only measured quantities and known physical constants, where XCT fundamentally

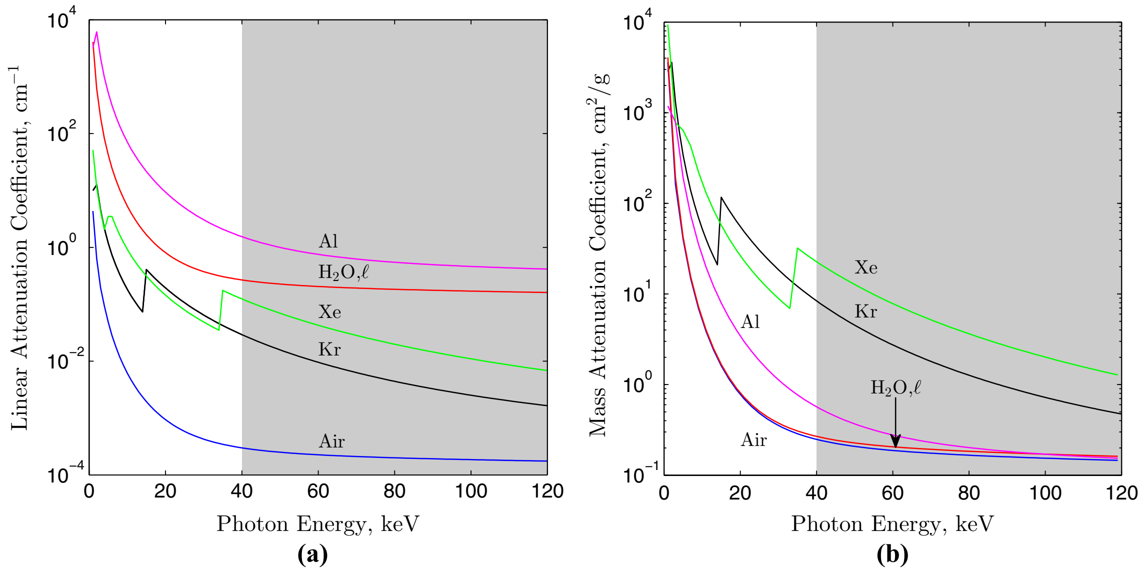

Fig. 2 Attenuation coefficients of representative materials versus photon energy; *shading* shows energy range of clinical XCT (*color online*). **a** Linear attenuation coefficients. **b** Mass attenuation coefficients

measures $\bar{\mu}$. Finally, substitution of Eq. (10) into Eq. (11) directly relates the mole fraction to the measured attenuation $\bar{\mu}_M$ through the following linear mixing law,

$$X_1 = \frac{\bar{\mu}_M - \bar{\mu}_2}{\bar{\mu}_1 - \bar{\mu}_2}, \tag{12}$$

where $\bar{\mu}_1$ and $\bar{\mu}_2$ are the measured linear attenuation values of components 1 and 2 at pressure P and temperature T. This result not only emphasizes the ease with which binary gas-phase mixture composition can be measured at constant temperature and pressure via XCT, but also points to the potential utility of a first-principles analysis in allowing for simultaneous measurements of several different quantities of interest. This last point will be expanded upon in Sect. 5.

3 XCT diagnostics for gas-phase fluid phenomena

3.1 Theoretical implications for experimental design

The analytical framework developed in Sect. 2.3 could theoretically be applied to measure scalar transport in any number of gas-phase flows if X-ray diagnostic systems were sensitive enough to detect changes in attenuation resultant from variations in the composition or density of any gaseous compound of interest. In reality, however, such diagnostics will be contrast-limited because most ambient gases are extremely non-attenuative at energies characteristic of clinical scanners (40–120 keV). Thus, because gas densities will always be orders of magnitude lower than those of other phases normally imaged via clinical XCT, it is necessary to utilize a high-ξ gas for gas-phase measurements. In light of this requirement, krypton gas was chosen as the working fluid for this study due to its high mass attenuation coefficient, chemical inertness, relatively low cost (compared to other gases with these qualities), and lack of health hazards. Krypton has previously been used with great success as a contrast agent in XCT studies of pulmonary absorption in the medical field (Simon 2005) and rock porosity in the context of petroleum engineering (Vega et al. 2014). Linear and mass attenuation coefficients for krypton and other pertinent materials are illustrated in Fig. 2. Note that the sharp discontinuities observed in the curves for krypton and xenon occur at energies characteristic of the inner K electron shells of each atom; at these energies, a sharp jump in attenuation is observed because incoming photons begin to contain enough energy to interact with K-electrons via the photoelectric effect (Macovski 1983).

Demonstrating the viability of XCT as a diagnostic tool for gas-phase fluid mechanics is best accomplished using a well-known flow configuration. Gas-phase jet flows represent a classic test case for a wide variety of diagnostics, and for tomographic methods in particular, because they are relatively simple to set up while being theoretically, experimentally, and computationally well characterized (Birch et al. 1978; Dowling and Dimotakis 1990; Emmerman et al. 1980; Mi et al. 2001; Su et al. 2010; Watt and Vest 1990; Yip and Long 1986). Further, the jet geometry is useful in avoiding such requirements as confinement in a flow passage, which would complicate initial investigation of the diagnostic by introducing potential sources of

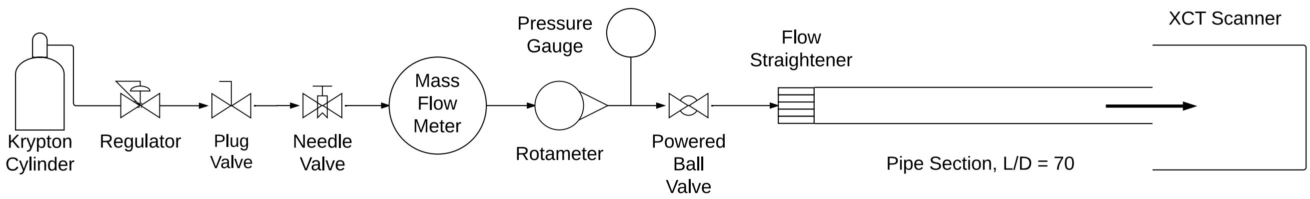

Fig. 3 Schematic of experimental setup

interference or artifacts into the XCT scans. Vertical gaseous jets are especially common in experimental work due to symmetry, well-developed similarity laws, and ease of setup (Chen and Rodi 1980), but the geometry of common clinical XCT scanners requires the use of a horizontal jet. While experimentally convenient for the present work, however, a horizontal krypton jet exhausted into ambient surroundings will by nature be negatively buoyant due to the high specific gravity of krypton. Negatively buoyant inclined and horizontal jets have been previously studied, often in the context of submerged liquid discharges (Fan 1967; Jirka 2004; Papakonstantis et al. 2011), but literature on such flows in gas-phase phenomena is sparse (Britter 1989; Wang and Andreopoulos 2010). Buoyancy effects in vertical jets, however, have been well characterized experimentally (Chen and Rodi 1980; Panchapakesan and Lumley 1993; Papaniclaou et al. 2008; Pitts 1991).

3.2 Experimental design and facility specifications

All experiments were performed on a GE HiSpeed CT/i XCT scanner using a fan-beam geometry. This fan-beam geometry, wherein axially thin (effectively one dimensional) projections are reconstructed in two dimensions at different positions and then stacked to form a three-dimensional reconstruction, is typical of clinical XCT scanners. Use of a cone-beam geometry, wherein many slices can be reconstructed simultaneously from a series of two-dimensional projections, would also have been an acceptable choice—in this particular study, the fan-beam geometry was a function of facility constraints as opposed to a particular experimental design. Several calibration scans were undertaken to determine the best scan parameters at which to run each experiment. Native software was used for tomographic reconstruction. The experimental apparatus, illustrated in Fig. 3, consisted of a krypton gas cylinder connected to a long tube section via a plug valve, metering valve, mass flowmeter, and actuated ball valve. The flow was controlled by adjusting the metering valve to a particular setting and varying the pressure supplied by the krypton regulator such that desired values were read by the mass flowmeter. In this way, flow conditions could be precisely replicated over a long series of trials. Alignment of the pipe and jet exit with the axis of the XCT scanner to within 0.4 degrees was performed using laser sights built into the scanner and confirmed via scout scans of the entire apparatus.

A set of two different jet characterization experiments was performed by exhausting a krypton jet from a copper tube of 76.2 cm in length with an inner diameter of $D = 1.09$ cm, resulting in a development length of approximately 70 D for the pipe flow. A flow straightener was placed at the entrance to the tube to ensure a well-developed pipe flow. This experimental setup was used to create several datasets describing a krypton jet exhausted into ambient air at bulk velocity of $u_o = 9.5$ m/s. This results in an exit Reynolds number of $Re_o = 16{,}000$ with Re_o defined as,

$$Re_o = \frac{u_o D}{\nu_o}, \tag{13}$$

where the subscript o indicates reference to the condition at the exit orifice. All scans were performed at a tube voltage of 80 kVp,[1] a tube current of 200 mA, 1 mm axial resolution, and 200 µm in-plane resolution. Each axial slice was reconstructed over a radial domain of 10 cm in diameter using 972 views taken over a total time of 1 s. Flow rate data from an Aalborg GFM flowmeter and ambient temperature data from a type K thermocouple were logged using LabView software. Further, the actuated ball valve was controlled in such a way that flow could be stopped or started immediately from the LabView console. These experiments were made viable in terms of krypton usage by utilizing the custom control and valve system to allow for on-demand creation of well-controlled, constant-velocity jets at relatively low flow rates.

The first jet experiment involved obtaining ten scan sets consisting of 67 axial slices of 1 mm axial depth at 3 mm spacing over a 20 cm domain. These ten full-length scans

[1] The term “kVp” is standard notation for “kilovolts peak,” which determines the maximum energy in keV of a single photon accelerated by the X-ray tube. The photon beam will realistically have a polyenergetic distribution with the maximum energy value in keV determined by the kVp value of the tube.

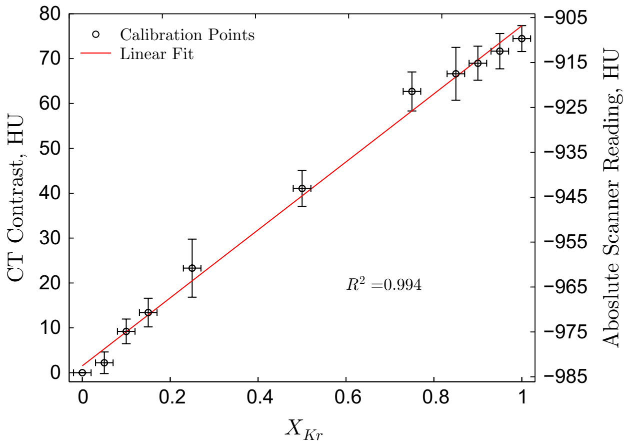

Fig. 4 Krypton XCT calibration curve; *vertical* and *horizontal bars* indicate 95 % confidence intervals

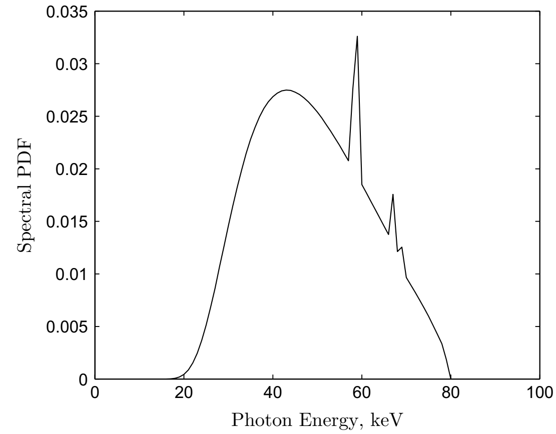

Fig. 5 GE HiSpeed CT/i theoretical spectrum calculated from SpekCalc (Poludniowski et al. 2009)

were conducted in order to allow for nearly continuous spatial coverage of the jet while obtaining a large enough sample size for useful multiple-trial averaging. Importantly, this first set of experiments was conducted using the scanner's baseline calibration settings that are based on measurements of a water phantom, while later experiments utilized an air-based calibration that improves data quality.

The second experiment involved obtaining more detailed data at five specific axial locations, each of which was scanned 20 times in order to enhance statistical convergence of the results. Moreover, minimization of imaging artifacts via the combination of air-based calibration and background subtraction allows for faithful quantitative reconstruction of the jet fluid concentration field for this dataset. Pertinent results from each of these experiments, along with a full discussion of the detailed air calibration data, can be found in the following sections.

3.3 Presentation of detailed calibration data

In order to fully characterize scanner behavior and allow for accurate quantitative interpretation of the data, a set of detailed calibration data describing scanner response to various krypton mole fractions was obtained. In particular, it is important to ensure that the detector operates in linear fashion in the low-contrast region we consider in order to implement the linear mixing law of Eq. (12) with confidence. The calibration curve illustrated in Fig. 4 was created using five scans of thin plastic balloons filled to various krypton concentrations using a pulmonary syringe with air as the bath gas. Error bars in Fig. 4 are 2 % for the mole fraction measurement (horizontal direction) and the 95 % confidence interval of the XCT measurements over all reconstructed voxels in all five scans, assuming a Gaussian distribution on the variation (vertical direction). Reasonably linear behavior in agreement with the theory is observed throughout the domain, and most notably even in the case of 5 % krypton mole fraction, indicating that the scanner is indeed sensitive enough to allow for resolution of a wide domain of krypton mole fractions. Note that the path length in the calibration scans was 20 cm through the various krypton–air mixtures inside the balloons, while in the jet experiments, the path length through the gas mixture would be between 1 and 5 cm with krypton concentration depending on spatial position.

To compliment this calibration procedure, data from the X-ray tube manufacturer (Dunlee) were used in combination with the SpekCalc software package (Poludniowski et al. 2009) to compute a theoretical spectrum for the XCT device. This probability density function, reproduced in Fig. 5, can be used to compute a theoretical value for the dynamic range in the denominator of Eq. (12), which can be compared to the value obtained via direct calibration. Note that the sharp peaks in the spectrum result from characteristic radiation concentrated at energies analogous to the transition energies between electron orbitals in the tungsten target (Prince and Links 2006).

It is apparent from Fig. 4, for instance, that we report the average CT number for pure krypton as −911 HU while air registers at an average of −985 HU, which is higher than the value of −998 HU predicted by the CT theory using Eqs. (2) and (3) along with the spectrum illustrated in Fig. 5. Similarly, the measured value of krypton at −911 HU compares reasonably to the theoretical value of −903 HU computed using scanner hardware data and SpekCalc. This type of discrepancy is not unexpected given that we are operating in the extreme low-contrast regime of the scanner, and that the constant offset error between theoretical and experimental attenuation values when measuring pure air is often on the order of 10 HU, even for newer scanners (ImPACT Group 2009). These differences are mostly the result of the clinical context of most XCT scanners, wherein internal reconstruction parameters are optimized for reconstruction of water phantoms. However, despite this slight misalignment between theoretical attenuation results and actual scanner readings, the calibration data of Fig. 4 allow us to utilize Eq. (12) in the following manner on a voxel-by-voxel basis,

$$X_{\mathrm{Kr}} = \frac{\bar{\mu}_{\mathrm{Meas}} - \bar{\mu}_{\mathrm{Bk}}}{\bar{\mu}_{\mathrm{Kr}} - \bar{\mu}_{\mathrm{Air}}}, \tag{14}$$

where $\bar{\mu}_{\mathrm{Meas}}$ is the jet experiment reading, $\bar{\mu}_{\mathrm{Bk}}$ is the reading from a background scan taken with only air in the scanner, $\bar{\mu}_{\mathrm{Kr}}$ is the average krypton CT number from the balloon calibration procedure, and $\bar{\mu}_{\mathrm{Air}}$ is the average air CT number from the balloon calibration procedure. Note that this transformation can also be directly implemented via Eq. (11) if the polyenergetic scan spectrum and the scanner air offset are well known.

As a final point, note that these calibration scans were performed in an *optically opaque* environment, which is one of the great potential advantages of gas-phase XCT. While the remainder of the results presented in this paper were collected in an optically accessible setup (i.e., there was no optical obstruction in the experimental apparatus), similar results could easily be obtained without optical access. A notable complication for some optically inaccessible measurements would be the case of beam hardening, in which very attenuative outer materials can preferentially attenuate low-energy photons, leading to reconstructed attenuation measurements that are too high in the interior of a subject. The present study avoids beam-hardening issues via experimental design, but these artifacts could be corrected in future experimental situations where beam hardening would be unavoidable using modern XCT calibration and postprocessing techniques (Heindel 2011; Hsieh 2009).

3.4 Uncertainty analysis

When evaluating the various results presented here, it is important to understand associated measurement uncertainties. Uncertainties associated with gas-phase XCT can be placed into several categories: intrinsic detector variation error, systematic reconstruction error, flowfield fluctuation error, and physical noise mechanisms. Each of these is explored below in detail (Boas and Fleischmann 2012; Prince and Links 2006).

3.4.1 Intrinsic detector variation error

The first type of error that one would consider in an experimental system is the variation caused by non-uniform hardware operation. The manufacturer of the GE HiSpeed CT/i scanner used in this experiment reported a nominal standard deviation of ±3 HU on a voxel-by-voxel basis. As reflected in Fig. 4, standard deviations were generally below 2 HU in each individual scan in the dataset presented here. Note that this standard deviation remains constant regardless of the number of scans considered, and that there exists minimal correlation between standard deviation and CT number. Thus, we conservatively take the measurement error due to random detector variation as $\sigma_{\mathrm{Det}} = 2$ HU.

In addition to random detector variation, a systematic decay in detector response over time was observed in the facility used for these experiments that resulted in an average decrease of 0.04 HU per scan within the region of interest as subsequent scans were conducted. This type of detector response drift is particularly common in fan-beam geometries because there is usually no detector element that consistently receives an unattenuated signal that can be used for self-calibration of the detector array at each point in time (Macovski 1983). Because the high-concentration segment of the calibration data in Fig. 4 was taken at the end of a nearly 120-scan routine, we take the CT contrast reported in Fig. 4 to be the baseline "warm scanner" value and adjust the value used for $\bar{\mu}_{\mathrm{Kr}}$ in Eq. (14) using a linear approximation,

$$\bar{\mu}_{\mathrm{Kr}} = \bar{\mu}_{\mathrm{Kr}}^{\mathrm{Cal}} - 0.04n, \tag{15}$$

where $\bar{\mu}_{\mathrm{Kr}}^{\mathrm{Cal}}$ is the value obtained from calibration and n is the number of scans previously performed in a given trial. The numerical value of the detector drift was confirmed by scanning a krypton balloon 150 consecutive times with an initially cool scanner. Importantly, we found the value of the drift to be dependent on the distance from the center of the reconstructed domain, but utilize the 0.04 HU value observed along the centerline in these calculations in order to simplify the analysis procedure while ensuring that the centerline mole fraction is accurately represented. We account for any potential error that this treatment may introduce by conservatively taking the resultant uncertainty as $\sigma_{\mathrm{Deg}} = 1.25$ HU.

3.4.2 Reconstruction error

Reconstruction error in some sense represents a systematic analog to detector variation. Specifically, error caused by low view numbers, systematic detector channel error, beam hardening, and other sources can cause so-called XCT artifacts to appear in the reconstructed field data. Given that we are operating near the lower limit of the scanner's contrast range, even small systematic detector errors can be quite significant in our results. In particular, when a single detector channel consistently over- or under-reports photon counts, this error propagates along a straight line in each projection, which results in a ring-shaped artifact in the reconstruction (Hsieh 2009; Prell et al. 2009). It is in fact quite common for XCT scanners to introduce these "ring artifacts," which represent axisymmetric variations in the reconstructed field output at particular radii, into the data due to the aforementioned geometric impossibility of detector self-calibration during the course of an examination (Macovski 1983). Such ring artifacts are well known in the XCT literature and can result from a myriad of sources including, but not limited to, local temperature variations, radiation damage, and different scintillator thicknesses (Prell et al. 2009; Sijbers and Postnov 2004). A wide literature on the removal of XCT artifacts exists, though most algorithms were not originally intended for application to extremely low-contrast situations such as that described here. Nonetheless, the state-of-the-art ring correction in polar coordinates (RCP) algorithm detailed in Prell et al. (2009) seems to apply well to this case and has thus been implemented to remove spurious artifacts from the data when appropriate. Note that the air-calibrated results for the second experiment from which we extract detailed quantitative krypton mole fraction data do not require this correction, but that it is useful in processing the results of the first jet experiment, which used the baseline water-based scanner calibration.

3.4.3 *Flowfield fluctuation error: analysis of time-varying XCT*

A third source of potential error stems from the fact that XCT reconstruction is performed using a set of projections that represent integral images of a temporally varying field at slightly different points in time. In this case, reconstructions for each axial slice were computed from 972 linear projections taken over a total time period of 1 s, meaning that a scan of the full domain (67 slices during the first experiment) took just over 1 min. Note that the scanner used in this study only outputs reconstruction (not projection) data, meaning that all analysis performed here references exclusively reconstruction data. Thus, it is important to note that the reconstructions presented here are "time-averaged" in the sense of Heindel (2011) in that while each projection is recorded at a timescale on the order of a millisecond, the reconstruction is computed from a set of 972 projections that took a total of 1 s to record.

The fact that clinical XCT scanners utilize a single rotating source-detector pair requires that reconstructions be based on projection data acquired at different time increments, as described above. Errors associated with XCT reconstruction of time-dependent data were analyzed by Willis and Bresler (1990). For this particular application, a simplified approach was pursued to assess how the Radon transformation performs on a transient signal. For this, we considered a disk with diameter of 1 cm and unity attenuation coefficient that homogeneously oscillates with frequencies up to 10 kHz and magnitude of 0.2 commensurate with the expected jet turbulence intensity I_T. The reconstructed results were compared to those of a static disk at the corresponding mean field. It was observed that the average voxel-to-voxel error was below 1 % of the mean field for frequencies not in phase with the projection sampling frequency, and, further, that there was no directional bias to these errors. Thus, these results suggest that temporal variations should not contribute to systematic error in this study because it is focused on resolution of the mean field, but that this issue should certainly be considered in experimental design and data interpretation from future XCT studies that intend to interrogate non-stationary aspects of turbulent flows.

We can obtain useful quantitative insight into this issue by comparing the characteristic timescales of the system under consideration. The timescale defining the axial slice scan time, τ_{Scan}, can be approximated as,

$$\tau_{\mathrm{Scan}} \sim 1 \ \mathrm{s}, \tag{16}$$

from observed scanner operation. The large-eddy turnover time, τ_{E}, would be the appropriate metric for defining the timescale over which large-scale turbulent fluctuations occur. We can estimate this quantity in terms of representative values of an integral length scale L, turbulence intensity I_T, and a velocity scale. Taking $L \sim D$, a reasonable value of $I_T \approx 0.2$ along the centerline (Birch et al. 1978; Panchapakesan and Lumley 1993; Pope 2000), and u_o as an applicable velocity scale yields,

$$\tau_{\mathrm{E}} \sim \frac{D}{I_T u_o} = 0.005 \ \mathrm{s}. \tag{17}$$

In this case, we see that the ratio between the scan and eddy turnover timescales is approximately,

$$\frac{\tau_{\mathrm{Scan}}}{\tau_{\mathrm{E}}} \sim O\left(10^2\right), \tag{18}$$

meaning that the timescale over which projections are taken is several orders of magnitude longer than that on which large-scale turbulent fluctuations occur. Due to the difference in scales between the total scan time and eddy turnover times, a full set of projections contains data from over 100 eddy turnovers. Thus, data in a given projection should be minimally correlated in time with data from the majority of the other projections (taken during different eddy turnovers) that contribute to the reconstruction. This result implies that reconstructing a field from these projections would lead to a reasonable estimation of the statistically converged mean field (Heindel 2011). Averaging over many uncorrelated reconstructions as we do in the present work further mitigates any error introduced via reconstruction of the stationary mean field from instantaneous projections taken at different times. Nonetheless, we conservatively estimate the measurement variation resultant from this phenomenon as $\sigma_{\mathrm{Turb}} = 2$ HU to account for any non-stationarity in the reconstruction of the time-varying flowfield.

3.4.4 Photon noise

In most XCT modalities, Poisson-distributed variation from the photon generation process is a dominant source of noise (Macovski 1983). However, in the context of low-attenuation gas-phase flows, photon counts will be quite high, and thus the variance of this Poisson distribution, σ^2_{Pho}, will be small compared to variations in attenuation resulting from fluctuations in the turbulent flowfield. We therefore assume $\sigma_{\mathrm{Pho}} = 0$ HU in our error estimates.

3.4.5 Standard error estimation

Considering the sources of potential uncertainty presented above, we construct an estimation of the measurement variance that will be used to create error bars for quantitative krypton mole fraction measurements. A general estimation of the variance would combine contributions from all potential sources as follows, where we have assumed that uncertainty introduced via detector degradation is not mitigated by the averaging procedure (i.e., does not vary inversely with scan number n),

$$\sigma^2_{\mathrm{Tot}} = \frac{\sigma^2_{\mathrm{Det}} + \sigma^2_{\mathrm{Pho}} + \sigma^2_{\mathrm{Turb}}}{n} + \sigma^2_{\mathrm{Deg}}. \tag{19}$$

Note that we would separately consider systematic errors such as artifacts in this framework. Using values estimated above for contributions to the total error from these different sources, we can estimate the standard error of the mean of n measurements of the average krypton mole fraction at each pixel over a 75 HU dynamic range, $\mathrm{SE_n}$, as,

$$\mathrm{SE_n} = \frac{1}{75\ \mathrm{HU}} \sqrt{\frac{\sigma^2_{\mathrm{Turb}} + \sigma^2_{\mathrm{Pho}} + \sigma^2_{\mathrm{Det}}}{n} + \sigma^2_{\mathrm{Deg}}}. \tag{20}$$

Note that contributions to $\mathrm{SE_n}$ arising from σ_{Turb}, σ_{Pho}, and σ_{Det} can be controlled by increasing the number of scans. In this study, we have chosen $n = 20$ in order to ensure that the reported standard error of $\mathrm{SE_{20}} = 0.02$ is relatively insensitive to uncertainties in the estimates of σ_{Turb}, σ_{Pho}, and σ_{Det}. We utilize this estimate of the standard error when presenting intentionally conservative error bars on experimental measurements in later sections. Indeed, many of these values are reported as azimuthal averages over many pixels, and thus, these error bars will be particularly conservative given that additional reduction in standard error resultant from azimuthal averaging is not considered.

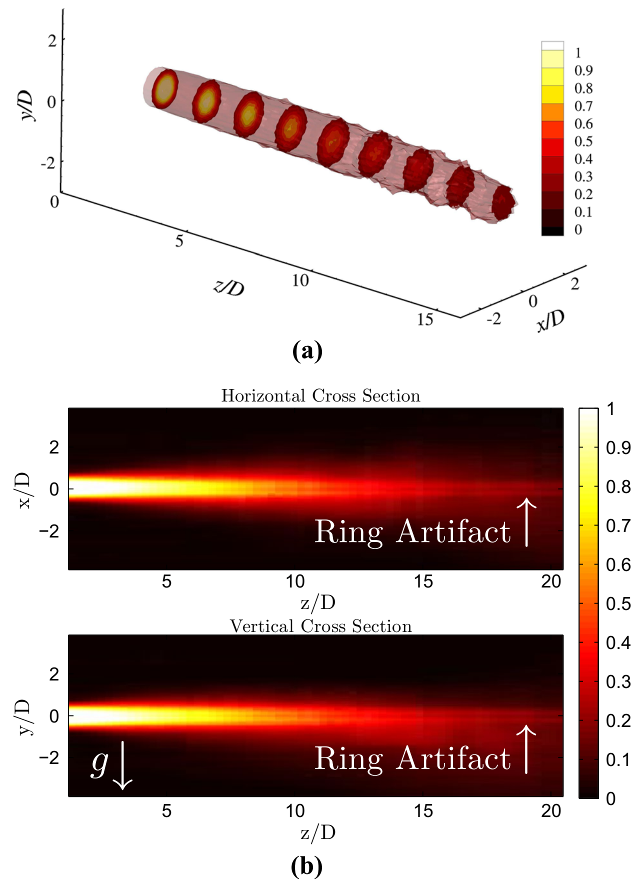

Fig. 6 XCT visualizations of the krypton jet concentration field. **a** Isosurface at $\langle X_{\mathrm{Kr}} \rangle_{10} = 0.25$ and axial cross sections. **b** Horizontal (*top*) and vertical (*bottom*) $\langle X_{\mathrm{Kr}} \rangle_{10}$ cross sections

4 Results and discussion

4.1 Full-length jet visualization and buoyancy analysis

We now proceed to analyze the data from the first jet experiment, which was conducted using the baseline water-phantom calibration for the XCT scanner. In the following sections, it will be useful to present several different types of X_{Kr} data. We therefore utilize $\langle X_{\mathrm{Kr}} \rangle_{\mathrm{n}}$ to represent krypton mole fraction averaged over n reconstructions, $\langle X_{\mathrm{Kr}} \rangle_{\theta}$ to denote an average in the azimuthal direction, and $X_{\mathrm{Kr,C}}$ to indicate mole fraction along the jet centerline. To illustrate the level of detail obtained from this diagnostic, we present a 3D reconstruction of average data from the first experiment over ten scans in Fig. 6. Note in particular the well-visualized inner structure of the jet as well as the effective capture of the jet buoyancy effect as the outer isosurface begins to bend in the downward direction near the far portion of the axial domain. This trend is apparent both in the 3D data and in the relative shapes of the horizontal and vertical cross sections, as the horizontal cross section remains symmetric, while the vertical cross section has higher krypton mole fractions in the direction of gravity.

It is also apparent from these data that scans using the baseline water-phantom calibration result in a noticeable ring artifact near the center of the domain, which can be observed as two lines symmetrically placed about the center of the horizontal and vertical cross sections. Thus, as mentioned above, we have applied the RCP filter of Prell et al. (2009) to mitigate the effects of these errors on our reconstructed fields for results from the first experiment. To understand the errors that this routine, which is fundamentally based on intelligent application of median filters and thresholding, might introduce, we present in Fig. 7 a comparison between an unfiltered and a filtered dataset describing the radial krypton mole fraction profile at $z/D = 10$ along the vertical centerline of the jet. Several key observations arise from these data. First, the filter performs well in eliminating noise resultant from ring artifacts near the outer region of the jet, as the line traces the appropriate smooth curve through the original unfiltered data. Note that these small ridges near the outer part of the y-domain in Fig. 7 can be directly correlated with rings in the axial cross sections of these data. Further, the ring artifact near the center of the jet (visible as a small depression in Fig. 7 near $y/D = 0$) remains throughout this particular dataset. Fundamentally, this occurs because pixel count decreases with radius from the center of the jet, meaning that the filter has fewer uncorrupted pixels over which to take a median near the center of the domain. We show in later results that this type of error can be mitigated via rigorous calibration procedures.

Despite the existence of the central ring artifact, this dataset can nonetheless give useful qualitative and quantitative insight into the effects of buoyancy on the heavy gaseous jet. For instance, Becker and Yamakazi (1978) analyze the behavior of a propane jet diffusion flame using a non-dimensional coordinate that can be approximated as (See and Ihme 2014),

$$\zeta \approx \frac{z}{D}\left(\frac{\rho_\infty}{\rho_o} Fr^{-2}\right)^{1/3}, \tag{21}$$

where z is defined from the jet orifice and $Fr = u_o/\sqrt{gD}$ with g the gravitational constant. The criterion $\zeta < 1$ is applied to define the forced convection limit wherein buoyancy effects are negligible. While the situation modeled here is certainly different in character than that of the vertical alignment of Becker and Yamakazi (1978) in the sense that gravity does not directly oppose the motion of the fluid, we can nonetheless use this criterion as an estimate of the point at which buoyancy becomes important in this flow. Setting $\zeta = 1$ and solving for the location at

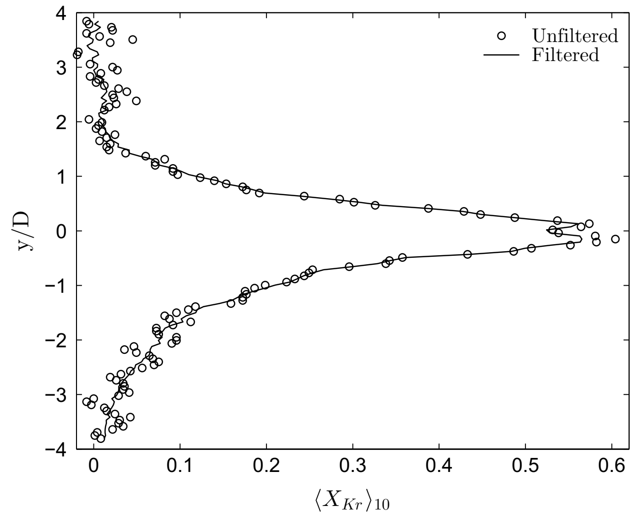

Fig. 7 Effect of RCP filter on $\langle X_{\mathrm{Kr}}\rangle_{10}$ data for radial profile at $z/D = 10$

which buoyancy becomes important yields a critical value of $z/D \sim 14$. Qualitative agreement with this trend is best observed in Fig. 6. Note the expected symmetry in jet development out to just before $z/D = 10$ before substantial downward-biased asymmetric spreading begins to occur between $z/D = 10$ and $z/D = 15$. The work of Pitts (1991) demonstrates that the jet density ratio may significantly affect the measurement of the virtual origin, and thus, we perform only a brief analysis here to illustrate approximate qualitative agreement between this experiment and the buoyancy criterion of Becker and Yamakazi (1978).

4.2 Quantitative analysis of jet concentration data: comparison to computational results and additional measurements

As a final piece of analysis for this experiment, we extract krypton mole fraction profiles from the second jet experiment and compare these data to relevant experimental and computational results. This dataset was obtained after air-based scanner calibration and was recorded within 24 h of the original balloon calibration experiment, meaning that the scanner behavior exactly replicates that observed in Fig. 4. Both calibration and jet data indicate the absence of persistent ring artifacts—such behavior is expected given that the air calibration conditions are much closer to actual operating conditions than water-phantom calibration conditions would be. This implies that systematic detector channel errors should be smaller in the former case. Further, the dataset describing 150 consecutive scans of a krypton balloon (previously used to investigate detector drift) indicates that the majority of gains in terms of noise reduction are observed within the first 10–20 scans,

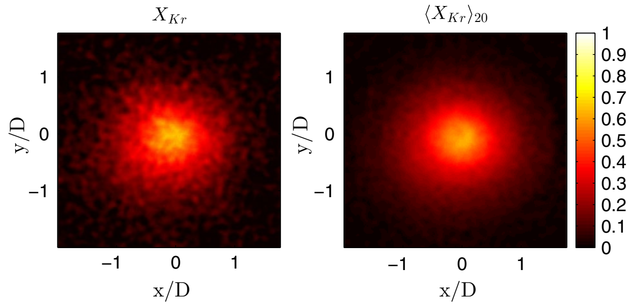

Fig. 8 Comparison of X_{Kr} and $\langle X_{\mathrm{Kr}}\rangle_{20}$ at $z/D = 10$

with additional measurements contributing only marginally to better resolution of the mean field. Thus, in order to ensure reasonable statistical convergence of mean field measurements, 20 scans were taken at each of five axial locations ($z/D = 0.5, 2.5, 5, 10, 15$). Comparison of a single reconstruction to an average over twenty reconstructions is shown in Fig. 8.

Further, numerical integration of the reconstructed attenuation field commensurate with the mole fraction data at $z/D = 0.5$ indicates an estimated peak krypton absorbance of 0.025 through the centerline of the jet.[2] To arrive at this estimate, spectrally averaged linear attenuation coefficients were computed using Eqs. (2, 3), linear attenuation data from Fig. 2a, and the scanner spectrum from Fig. 5. Attenuation at each pixel was then computed from Eq. (10), and absorbance profiles were calculated directly via Eq. (5). Absorbance values were generally insensitive to the angle of line integration due to axisymmetry. We report the krypton absorbance as the difference between the centerline jet absorbance value and absorbance computed along a line containing pure air in order to specifically isolate the impact of the krypton.

Details of the large-eddy simulation (LES) and additional experimental data to which we compare the krypton jet XCT data from this study will now be discussed. Note that an LES was utilized instead of a RANS calculation in order to more accurately predict mixing in the turbulent environment characteristic of these experiments.

4.2.1 Large-eddy simulation details

To confirm our experimental results, a set of complementary large-eddy simulations were performed at the same conditions. A three-dimensional LES of the turbulent krypton–air jet at $Re = 16{,}000$ was computed using a structured LES-solver with a dynamic Smagorinski subgrid model (Germano et al. 1991). The computational domain was comprised of a structured non-uniform cylindrical mesh with approximately 3 million grid points ($542 \times 102 \times 64$ in the axial, radial, azimuthal directions, respectively) covering a spatial domain of 30 reference diameters in length and 10 reference diameters in radius. The numerical algorithm used to solve the variable-density Navier–Stokes equations utilizes a second-order accurate, finite-volume spatial discretization, and a predictor-corrector scheme is used for time advancement (Pierce and Moin 2004). The spatial grid was set up with non-uniform cell size in the axial and radial directions, with finer resolution in the shear layer and toward the jet orifice. The predictor-corrector method was implemented using two sub-iterations and a timestep size of 0.1 µs. Acceleration due to gravity is directly implemented in the $-y$ direction. The inlet of the domain comprises a fully developed turbulent pipe flow with mean velocity of u_{o} and a surrounding coflow with velocity of $0.05u_{\mathrm{o}}$. After six flow-through times (312 ms per flow-through), statistical results were collected through temporal averaging over two flow-through times. Mixture-averaged properties were used to describe molecular transport. Finally, it is worth noting that this algorithm has been parallelized for data exchange between processor units (4 nodes and 24 processors per node), which allows for faster LES run times.

4.2.2 Re-matched methane jet

We also compare data from the current experiment to that of Birch et al. (1978), who investigated an axisymmetric methane jet exhausted with a fully developed pipe flow profile at $Re = 16{,}000$. While the buoyancy and preferential diffusion aspects of the current setup are not replicated by the experiment of Birch et al. (1978), nearly all other parameters are exactly the same, making it a useful case to which to compare our data. Specifically, it is reasonable to expect axial concentration patterns to be relatively similar between the two jets (particularly at axial positions before buoyancy begins to take effect in the krypton jet). Radial profiles should show some level of qualitative agreement, but the radial data of Birch et al. (1978) are taken from the fully developed far field of the jet, whereas the krypton jet data will necessarily be taken from the near field. In general, though, this represents the most pertinent dataset in the literature and, crucially, contains data in the near field describing axial concentration decay.

4.2.3 Comparison of results

Results from computations, experiments, and the literature allow us to perform an analysis to confirm that the obtained XCT data reproduce species concentration profiles that are in agreement with results from other modalities. Figure 9a

[2] Absorbance is defined here as $\int \bar{\mu}\,\mathrm{d}s = -\ln(I_{\mathrm{d}}/I_0)$.

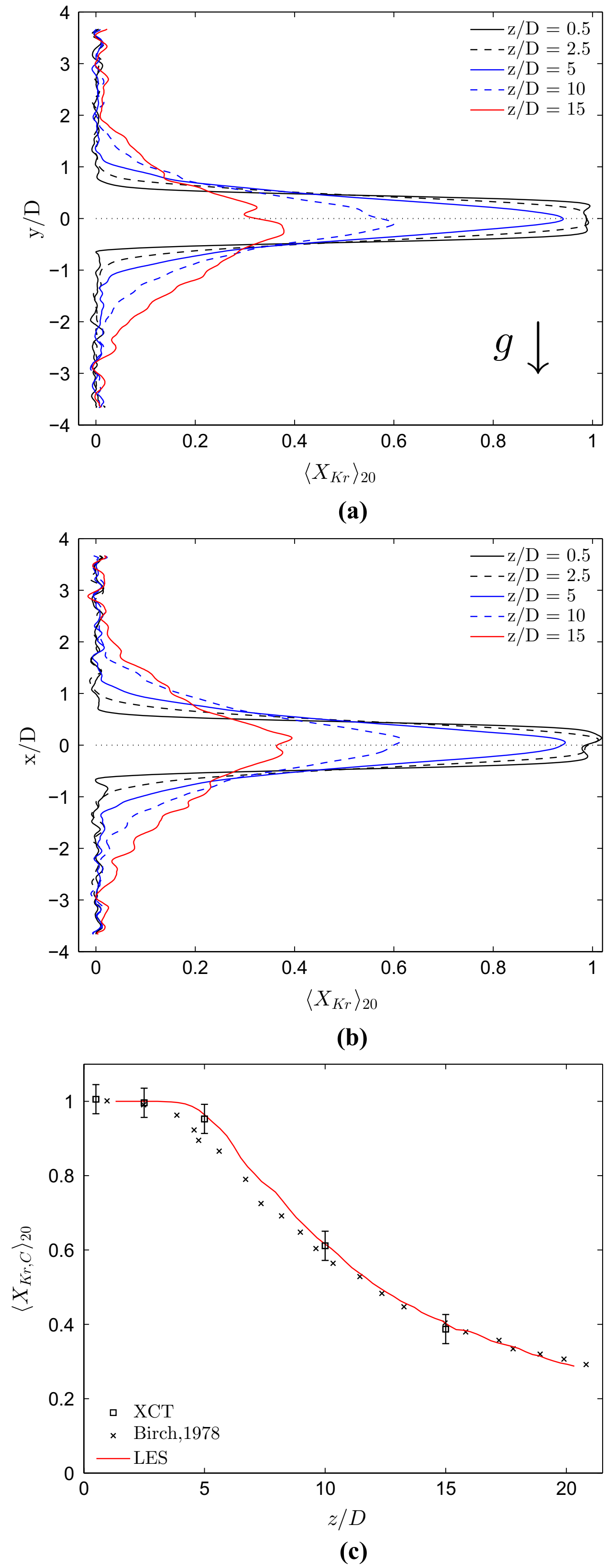

Fig. 9 Averaged $\langle X_{\mathrm{Kr}}\rangle_{20}$ profiles in **a** vertical, **b** horizontal, and **c** axial directions (*color online*)

illustrates vertical profiles of $\langle X_{\mathrm{Kr}}\rangle_{20}$ at the horizontal centerline, Fig. 9b shows analogous profiles in the horizontal direction, and Fig. 9c compares the mean centerline profile, $\langle X_{\mathrm{Kr,C}}\rangle_{20}$, from this experiment to that of a CH_4/air jet from the work of Birch et al. (1978) as well as to the LES computations. Note that each data point in Fig. 9 represents a single voxel that is $200\,\mu\mathrm{m} \times 200\,\mu\mathrm{m} \times 1$ mm in size in the horizontal, vertical, and axial direction, respectively. Figure 9a directly illustrates that the XCT data quantitatively capture the negative buoyancy of the jet, with profiles near the jet orifice being nearly symmetric before the heavy gas begins to sink toward the bottom of the jet at downstream positions. In particular, buoyancy is difficult to observe before $z/D = 10$, while the difference in the distance between the $z/D = 10$ and $z/D = 15$ profiles between the top and bottom portions of the jet is directly indicative of negative buoyancy. Note that data shown in Fig. 9a–c do not require utilization of the RCP ring artifact filter, with the only applied transformations being the linear mixing law of Eq. (14) to extract krypton mole fraction from the attenuation measurement and a moving average smoothing operation. Variations in the data observed in Fig. 9a near the centerline of the profiles for $z/D = 10$ and $z/D = 15$ result from the fact that the air scans used to compute $\bar{\mu}_{\mathrm{Air}}$ in Eq. (14) were conducted with a "cool" scanner, which gives smooth subtracted results at early scan times ($z/D < 10$), but causes the observed variation in computed $\langle X_{\mathrm{Kr}}\rangle_{20}$ near the centerline, where detector drift is most pronounced, at later times. Importantly, investigation of nearby pixels confirms that the peak krypton mole fraction value is minimally affected. For consistency, the same air background is used for all calculations performed here, but one could also work to create a temporally resolved air background if further precision was required. Note that subsequent quantitative comparisons feature azimuthally averaged datasets that eliminate much of the variation associated with these raw pixel measurements.

In Fig. 9c, we observe the expected general scaling of the maximum jet krypton mole fraction with $1/z$, even in the horizontal geometry, and see that the centerline concentration falloff takes a slightly different form in the krypton–air jet than in the lower density ratio methane–air jet. Encouragingly, the LES predicts the experimental centerline concentration decay nearly exactly. Note that error bars in Fig. 9c, as they do throughout this section, represent 95 % confidence intervals assuming Gaussian distribution of the overall error and the standard error estimate of Eq. (20).

Given that this dataset is comprised of measurements that fall in the near field of the negatively buoyant horizontal jet, detailed simulations of the jet near field provide a more useful basis for comparison of the radial profiles than

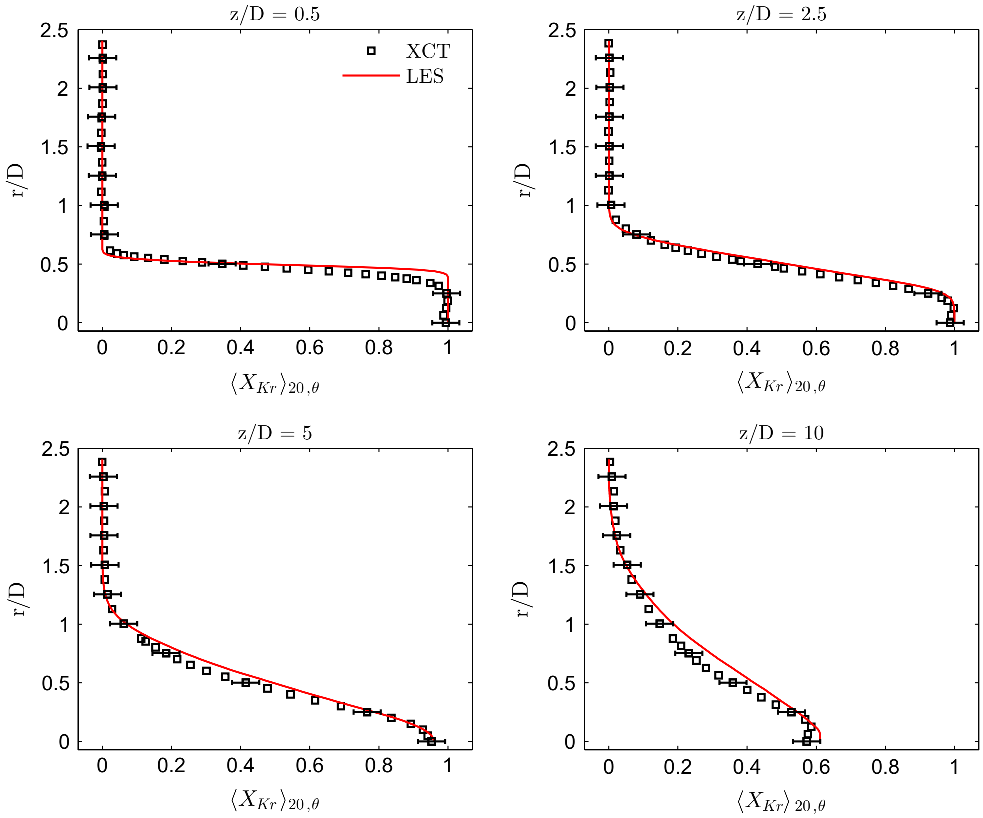

Fig. 10 Comparisons of azimuthally averaged radial $\langle X_{\mathrm{Kr}}\rangle_{20,\theta}$ profiles from experiments and simulations of the krypton–air jet

do the far-field self-similarity profiles generally reported in the literature for axisymmetric jets. Specifically, the radial profile data shown in Fig. 10 illustrate good agreement between experiments and LES results throughout the domain, and in particular for $z/D < 10$ where krypton mole fractions are high enough that we are not operating near the very bottom of the dynamic range of the XCT scanner. Overall, the good agreement observed among these various results demonstrates both the viability of XCT as a quantitative diagnostic for gas-phase flow and the usefulness of LES as a tool in performing validation studies for new diagnostics in non-standard flow situations.

5 Conclusions and future directions

We have demonstrated the successful application of clinical XCT methods to measuring gas-phase mole fractions in a time-varying turbulent flowfield. Through the use of radiodense krypton gas, it was possible to quantitatively and qualitatively visualize mixing of a negatively buoyant krypton–air jet. These results were validated through both comparison to previous literature and simulations of the experimental geometry. This diagnostic shows potential in allowing for easy tomographic visualization of mean scalar concentration fields using well-established and often easily accessible clinical XCT scanners. Further, its ability to extend these experiments to optically inaccessible setups that would be difficult to interrogate with other methods represents a potentially unique addition to the set of tools currently available in gas-phase experimental fluid mechanics.

We have also identified potential sources of uncertainty in this diagnostic, which arise from intrinsic detector variation, detector degradation, systematic reconstruction error, flowfield fluctuations, and physical mechanisms such as photon noise. Random detector variations are well documented and easily incorporated into our analysis, while temporal variability and artifact-induced reconstruction errors require more intensive consideration. Measurements of the mean flow will have errors that are fundamentally related to the relationship between scanner frequency and the underlying temporal power spectrum of the turbulent jet, but such errors are diminished via reconstruction using many uncorrelated projections and further averaging over multiple uncorrelated trials. Additionally, due to the low attenuation of gas-phase flows, photon fluence variations are not a major source of error in the gas-phase XCT results presented here. Finally, artifact errors are spatially localized and somewhat predictable, but need to be carefully treated to ensure that other quantitatively important data are not corrupted by standard filtering algorithms. At present, lower-magnitude artifacts near the edges of the reconstructed domain may be easily removed via the filter of Prell et al. (2009), providing substantial reduction in these spurious signals. However, the central ring artifact will often not be completely removed by this procedure. Nonetheless, we have shown that air-based calibration procedures can reduce both the probability and magnitude of error in individual detector elements.

This work has also illuminated several key advantages and limitations of XCT as applied to gas-phase flows. Specifically, XCT is a very attractive option due to its ease of setup, lack of optical access requirements, fast scan times, three-dimensional image reconstruction, well-streamlined data processing procedures, and high spatial resolution. However, current clinical XCT technology lacks the capability to explore statistical turbulence properties in gas-phase flows because the timescale of the turbulence is substantially faster than that of the scanner. Further, we are restricted to a dynamic range of approximately 75 HU in the present study, which to some degree limits signal-to-noise ratio and low-concentration resolution. This particular issue could be mitigated through the use of a heavier tracer gas, such as xenon, but would carry additional expense. One could also utilize specialized XCT systems that allow for lower-energy scans to be conducted, but these types of systems are less common and require substantially more effort for reconstruction.

In the end, it is hoped that the use of XCT for interrogating gas-phase scalar mixing in various fluid-flow situations will represent a useful new approach in experimental fluid mechanics. Demonstration of this technique and characterization of associated error sources, however, represent only a first step toward understanding the potential of this diagnostic. For instance, we can directly extend our previous theoretical analysis to the case of unknown temperature by considering scans performed at K different energy levels. For each scan energy level k, we can write an equation of the form of Eq. (10) such that,

$$\sum_{j=1}^{N} \bar{\xi}_{kj} X_j W_j - \frac{R_\mathrm{u} T}{P} \bar{\mu}_k = 0, \quad k = 1, \ldots, K. \tag{22}$$

If there exist N X-ray tracked components in a mixture, then, we could theoretically extract both temperature and composition simultaneously using X-ray data from scans at $K = N$ different energy levels and solving the following linear system at each voxel in a multiple-energy analog to conventional dual-energy scanning techniques (Bushberg et al. 2011),

$$\begin{bmatrix} \bar{\xi}_{11} W_1 & \bar{\xi}_{12} W_2 & \ldots & \bar{\xi}_{1N} W_N & -\frac{R_\mathrm{u}\bar{\mu}_1}{P} \\ \bar{\xi}_{21} W_1 & \bar{\xi}_{22} W_2 & \ldots & \bar{\xi}_{2N} W_N & -\frac{R_\mathrm{u}\bar{\mu}_2}{P} \\ \vdots & \vdots & \vdots & \vdots & \vdots \\ \bar{\xi}_{N1} W_1 & \bar{\xi}_{N2} W_2 & \ldots & \bar{\xi}_{NN} W_N & -\frac{R_\mathrm{u}\bar{\mu}_N}{P} \\ 1 & 1 & \ldots & 1 & 0 \end{bmatrix} \begin{bmatrix} X_1 \\ X_2 \\ \vdots \\ X_N \\ T \end{bmatrix} = \begin{bmatrix} 0 \\ 0 \\ \vdots \\ 0 \\ 1 \end{bmatrix}. \tag{23}$$

Note that no data other than measured quantities and known atomic or molecular parameters would be required to directly solve this system for the composition and temperature simultaneously. Further, this result is unique to gas-phase XCT (as opposed to XCT performed with liquids or solids) because the ideal gas law allows for the direct relation between temperature and density.

Of course, the sensitivity of a multispecies approach would depend on a variety of issues that highlight the importance of various points discussed in this paper. For instance, such a diagnostic would require the existence of substantially different absorption spectra for the various tracked species over the range of the utilized XCT energies in addition to X-ray sources with the ability to supply the narrow-spectrum radiation necessary to differentiate the multiple-energy measurements. It would also be important to know the values of $\bar{\xi}$ precisely, which requires either detailed knowledge of the polyenergetic spectrum, use of a narrow-band source, or extensive calibration. Further, it is apparent that there exist significant differences between attenuation values observed by clinical XCT scanners and those computed directly from the theory——thus, for this matrix to be well conditioned, more precise attenuation measurements than those presented here would be required. Finally, in order to implement this scheme, it would be imperative that the error metrics discussed above be well understood and that extensive care be taken to minimize various XCT artifacts that could affect the solution of the prescribed linear system. Thus, while challenges certainly exist, integrating temperature measurements with scalar concentration via multiple-energy scans represents a potentially useful extension of the gas-phase XCT method presented here for measuring non-isothermal scalar transport and is indicative of the wide variety of applications to which gas-phase XCT diagnostics may bring substantial utility in the future.

Acknowledgments Support from the NDSEG Fellowship Program, Bosch, and NASA (Award No. NNX15AE42A) is gratefully acknowledged. Discussions with Rebecca Fahrig on the experimental analysis of X-ray data are also much appreciated. We thank Volker Sick for valuable input on the manuscript. Finally, the advice and support of

John Eaton in creating the experimental setup were crucial to the success of this study.

References

Agrawal AK, Butuk NK, Gollahalli SR, Griffin D (1997) Three dimensional rainbow Schlieren tomography of a temperature field. Appl Opt 37(3):479–485

Becker HA, Yamakazi S (1978) Entrainment, momentum flux, and temperature in vertical free turbulent diffusion flames. Combust Flame 33:123–149

Bennett K, Byer RL (1984) Optical tomography: experimental verification of noise theory. Opt Lett 7:270–272

Birch AD, Brown DR, Dodson MG, Thomas JR (1978) The turbulent concentration field of a methane jet. J Fluid Mech 88(3):431–449

Boas FE, Fleischmann D (2012) CT artifacts: causes and reduction techniques. Imag Med 4(2):229–240

Britter RE (1989) Atmospheric dispersion of dense gases. Annu Rev Fluid Mech 21(1):317–344

Bushberg JT, Seibert JA, Leidholdt EM, Boone JM (2011) The essential physics of medical imaging, 3rd edn. Lippincott, Williams, and Wilkins, Philadelphia

Byer RL, Shepp LA (1979) Two-dimensional remote air-pollution monitoring via tomography. Opt Lett 4(3):75–77

Chaouki J, Larachi F, Dudukovic MP (1997) Noninvasive tomographic and velocimetric monitoring of multiphase flows. Ind Eng Chem Res 36(11):4476–4503

Chen CJ, Rodi W (1980) Vertical turbulent buoyant jets: a review of experimental data. Pergamon, Oxford

Coletti F, Benson MJ, Sagues AL, Miller BH, Fahrig R, Eaton JK (2014) Three-dimensional mass fraction distribution of a spray measured by X-ray computed tomography. J Eng Gas Turbines Power 136(5):051508

Crow SC, Champagne FH (1971) Orderly structure in jet turbulence. J Fluid Mech 48(3):547–591

Dowling DR, Dimotakis PE (1990) Similarity of the concentration field of gas-phase turbulent jets. J Fluid Mech 218:109–141

Elsinga G, Scarano F, Wieneke B, van Oudheusden B (2006) Tomographic particle image velocimetry. Exp Fluids 6:933–947

Emmerman PJ, Goulard R, Santoro RJ, Semerjian HF (1980) Multiangular absorption diagnostics of a turbulent argon-methane jet. Energy 85(2):70–77

Escudero DR, Heindel TJ (2014) Acoustic fluidized bed hydrodynamics characterization using X-ray computed tomography. Chem Eng J 243:411–420

Fan L (1967) Turbulent buoyant jets into stratified or flowing ambient fluids. Tech. Rep. KH-R-15

Feng J, Okamoto K, Tsuru D, Madarame H, Fumizawa M (2002) Visualization of 3D gas density distribution using optical tomography. Chem Eng J 86:479–485

Floyd J, Geipel P, Kempf AM (2011) Computed tomography of chemiluminescence (CTC): instantaneous 3D measurements and phantom studies of a turbulent opposed jet flame. Combust Flame 158:376–391

Frank JH, Shavorskiy A, Bluhm H, Coriton B, Huang E, Osborn DL (2014) In situ soft X-ray absorption spectroscopy of flames. Appl Phys B 117(1):493–499

Germano M, Piomelli U, Moin P, Cabot WH (1991) A dynamic subgrid-scale eddy viscosity model. Phys Fluids A Fluid Dyn (1989–1993) 3(7):1760–1765

Heindel TJ (2011) A review of X-ray flow visualization with applications to multiphase flows. J Fluids Eng 133(7):074,001

Hiller B, Hanson RK (1988) Simultaneous planar measurements of velocity and pressure fields in gas flows using laser-induced fluorescence. Appl Opt 27(1):33–48

Hsieh J (2009) Computed Tomography. Wiley, Colorado

ImPACT Group (2009) Comparative specifications–64-slice CT scanners. Tech. Rep. CEP08027, National Health Service

Jackson DF, Hawkes DJ (1981) X-ray attenuation coefficients of elements and mixtures. Phys Rep 70(3):169–233

Jirka GH (2004) Integral model for turbulent buoyant jets in unbounded stratified flows. Part I: single round jet. Environ Fluid Mech 4(1):1–56

Kastengren A, Powell CF (2014) Synchrotron X-ray techniques for fluid dynamics. Exp Fluids 55(3):1–15

Kastengren A, Powell CF, Dufresne EM, Walko DA (2011) Application of X-ray fluorescence to turbulent mixing. J Synchrotron Radiat 18(5):811–815

Lavinskaya EA, Martemianov S, Saulnier JB, Fomin NA (2006) Limited-projection laser tomography of combined gasdynamic flows. J Eng Thermophys 44(31):979–989

Linne M (2013) Imaging in the optically dense regions of a spray: a review of developing techniques. Prog Energy Combust Sci 39(5):403–440

Macovski A (1983) Medical imaging systems. Prentice Hall, Upper Saddle River

Meier GEA (2002) Computerized background-oriented Schlieren. Exp Fluids 33:181–187

Mi J, Nobes DS, Nathan GJ (2001) Influence of jet exit conditions on the passive scalar field of an axisymmetric free jet. J Fluid Mech 432:91–125

Mohamad EJ, Rahim RA, Ibrahim S, Sulaiman S, Manaf MS (2006) Flame imaging using laser-based transmission tomography. Sens Actuators A 127:332–339

Panchapakesan NR, Lumley JL (1993) Turbulence measurements in axisymmetric jets of air and helium. J Fluid Mech 246:225–247

Papakonstantis IG, Christodoulou GC, Papanicolaou PN (2011) Inclined negatively buoyant jets 2: Concentration measurements. J Hydraul Res 49(1):13–22

Papaniclaou PN, Papakonstantis IG, Christodoulou GC (2008) On the entrainment coefficient in negatively buoyant jets. J Fluid Mech 614:447–470

Pierce CD, Moin P (2004) Progress-variable approach for large-eddy simulation of non-premixed turbulent combustion. J Fluid Mech 504:73–97

Pitts WM (1991) Effects of global density ratio on the centerline mixing behavior of axisymmetric turbulent jets. Exp Fluids 11:125–134

Poludniowski G, Landry G, DeBlois F, Evans PM, Verhaegen F (2009) SpekCalc: a program to calculate photon spectra from tungsten anode X-ray tubes. Phys Med Biol 54(19):N433–N438

Pope SB (2000) Turbulent Flows. Cambridge University Press, Cambridge

Prell D, Kyriakou Y, Kalender WA (2009) Comparison of ring artifact correction methods for flat-detector CT. Phys Med Biol 54:247–253

Prince JL, Links JM (2006) Medical imaging signals and systems. Prentice Hall, Upper Saddle River

Richards CD, Pitts WM (1993) Global density effects on the self-preservation behavior of turbulent free jets. J Fluid Mech 245:417–435

Santoro RJ, Semerjian HG (1981) Optical tomography for flow field diagnostics. Int J Heat Mass Transf 24(7):1139–1150

See YC, Ihme M (2014) Effects of finite-rate chemistry and detailed transport on the instability of jet diffusion flames. J Fluid Mech 745:647–681

Sijbers J, Postnov A (2004) Reduction of ring artifacts in high resolution micro-CT reconstructions. Phys Med Biol 49:3881–3895

Simon BA (2005) Regional ventilation and lung mechanics using X-ray CT. Acad Radiol 12:1414–1422

Snyder R, Hesselink L (1988) Measurement of mixing fluid flows with optical tomography. Opt Lett 13(2):87–89

Stuck BW (1977) A new proposal for estimating the spatial concentration of certain types of air pollutants. J Opt Soc Am 67(5):668–678

Su LK, Helmer DB, Brownell CJ (2010) Quantitative planar imaging of turbulent buoyant jet mixing. J Fluid Mech 643:59–95

Thompson A, Vaughan D (2005) X-ray data booklet. Lawrence Berkeley National Laboratory, Berkeley

Vega B, Dutta A, Kovscek AR (2014) CT imaging of low-permeability, dual-porosity systems using high X-ray contrast gas. Transp Porous Media 101:81–97

Wang Z, Andreopoulos Y (2010) Density and compressibility effects in turbulent subsonic jets part 1: mean velocity field. Exp Fluids 48:327–343

Watt DW, Vest CM (1990) Turbulent flow visualization by interferometric integral imaging and computed tomography. Exp Fluids 8:301–311

Willis NP, Bresler Y (1990) Tomographic imaging of time-varying distributions. Proc SPIE Biomed Image Process 1245:111–123

Wright P, Garcia-Stewart CA, Carey SJ, Hindle FP, Pegrum S, Colbourne SM, Turner PJ, Hurr WJ, Litt TK, Murray SC, Crossley SD, Ozanyan KB, McCann H (2006) Towards in-cylinder absorption tomography in a production engine. Appl Opt 44(31):6578–6592

Yip B, Long MB (1986) Instantaneous planar measurements of the complete three-dimensional scalar gradient in a turbulent jet. Opt Lett 11(2):64–66